Journal of Orthopaedic Translation 45 (2024) 107–119

Contents lists available at ScienceDirect

Journal of Orthopaedic Translation

journal homepage: www.journals.elsevier.com/journal-of-orthopaedic-translation

Original Article

Tibial cortex transverse transport regulates Orai1/STIM1-mediated NO release and improve the migration and proliferation of vessels via increasing osteopontin expression

Lingchao Kong [a,f], Yangyang Li [b], Zhongfang Deng [c], Xiaoyu Chen [c], Yin Xia [d], Bing Shen [e], Rende Ning [f,***], Lesha Zhang [c,**], Zongsheng Yin [a,*]

[a] Department of Orthopedics, The First Affiliated Hospital of Anhui Medical University, Hefei, Anhui, PR China
[b] School of Basic Medical Sciences, Guizhou Medical University, Guiyang, Guizhou, PR China
[c] Department of Physiology, School of Basic Medical Sciences, Anhui Medical University, Hefei, Anhui, PR China
[d] Department of Anesthesiology, Anhui Provincial Children's Hospital, Hefei, Anhui, PR China
[e] Dr. Neher's Biophysics Laboratory for Innovative Drug Discovery, State Key Laboratory of Quality Research in Chinese Medicine, Macau University of Science and Technology, Taipa, Macao SAR, PR China
[f] Department of Orthopedics, The Third Affiliated Hospital of Anhui Medical University, Hefei, Anhui, PR China

ARTICLE INFO

Keywords:
Osteopontin
Proliferation
Store-operated calcium entry
Tibial cortex transverse transport
Vascular endothelial cells

ABSTRACT

Background: Diabetic foot is a major complication of diabetes. The bone transverse transport method could be applied in clinics for treatment, which could improve the metabolism of the tissues via lasting distraction forces. However, the process' specific regulating mechanism is still unknown.

Methods: Based on the notion that the healing of bones involves the recruitment of calcium ions, in this study, we established the model of tibial cortex transverse transport (TTT) on rats and then used tissue immunologic detection, such as the double fluorescent staining to explore the expression of the calcium channels' calcium release-activated calcium modulator 1 (Orai1)/stromal interaction molecule 1 (STIM1), which belong to the store-operated calcium entry (SOCE) signaling pathways on the tissues around the bone transport area. By using the laser capture microdissection (LCM) tool, we acquired samples of tissues around the bone and endeavored to identify pivotal protein molecules. Subsequently, we validated the functions of key protein molecules through in vitro and in vivo experiments.

Results: After protein profile analysis, we found the differentially expressed key protein osteopontin (OPN). The in vitro experiments verified that, being stimulated by OPN, the migration, proliferation, and angiogenesis of human umbilical vein endothelial cells (HUVEC) were observed to be enhanced. The activation of Orai1/STIM1 might increase the activity of endothelial nitric oxide synthase (eNOS) and its effect on releasing nitric oxide (NO). Subsequently, the migration and proliferation of the HUVECs are improved, which ultimately accelerates wound healing. These signaling pathway was also observed in the OPN-stimulated healing process of the skin wound surface of diabetic mice.

Conclusion: This study identifies the molecular biological mechanism of OPN-benefited the migration and proliferation of the HUVECs and provides ideas for searching for new therapeutic targets for drugs that repair diabetes-induced wounds to replace invasive treatment methods.

The translational potential of this article: The OPN is highly expressed in the tissues surrounding the TTT bone transfer area, which may possibly stimulate the activation of eNOS to increase NO release through the SOCE pathway mediated by Orai1/STIM1. This mechanism may play a significant role in the angiogenesis of diabetic foot's wounds promoted by TTT, providing new therapeutic strategies for the non-surgical treatment for this disease.

* Corresponding author.
** Corresponding author.
*** Corresponding author.
E-mail addresses: nrd192@qq.com (R. Ning), zhanglesha@ahmu.edu.cn (L. Zhang), yinzongsheng@sina.com (Z. Yin).

https://doi.org/10.1016/j.jot.2024.02.007
Received 21 November 2023; Received in revised form 31 January 2024; Accepted 26 February 2024

1. Introduction

Along with the increasing economic development and changes in working and living patterns, high-fat diets promote the increasing trend of the incidence of diabetes worldwide [1]. In recent years, the number of diabetes patients has increased to more than 500 million in globe. Among several complications of diabetes, the diabetic foot is one of the most serious in end-stage diabetes [2]. In the past, once the diabetic foot emerges due to infection, even necrosis, orthopedic surgeons often use the traditional treatment of amputation [2,3], which would severely affect the normal life and basic limb function of patients, thus reducing their quality of life. Therefore, the aim of diabetic foot treatment is beginning to improve local blood supply, promote wound healing, control infection, and so on, all of which have the benefit of increasing patients' quality of life [2,4].

The underpinning concept of tibial cortex transverse transport (TTT) germinated from the intricate tension-stress principle articulated by Ilizarov, a luminary in Soviet Union Orthopedics in a bygone era [5]. The first application of TTT by Shevtsov VI [6] was the treatment of lower extremity ischemia induced by thromboangiitis obliterans [7]. Later, TTT was further applied to repair wounds caused by diabetic foot [8–11]. The principle is that through sustained tension, the cellular metabolism within and around the surgical area could be improved and the regeneration and repair of tissues could be accelerated [12–14]. However, there exist disputes and shortcomings regarding fenestration on healthy bones and the use of an external fixation stand for bone transporting—this could lead to certain extra costs, which increase the economic burden on patients and complications such as iatrogenic fractures or infections caused by improper care of pinholes [15]. Therefore, we aim to study the pathophysiological processes of transverse bone transport, focusing on the signaling pathways and molecular mechanisms that regulate microvascular proliferation, in the hopes of finding new therapeutic targets to replace traumatic treatment modalities.

Drawing from the animal models by Yang Y et al. [16,17], we established a tibial cortex transverse bone transport model in rats. Furthermore, we detected and analyzed the differentially expressed vascular-growth-promotion-related factors and then directionally captured the positive-expressed area by performing laser capture microdissection (LCM) [18]. Finally, we identified a key molecule, osteopontin (OPN), through proteomic analysis. Related research [19,20] indicates that OPN is a functional protein that not only stimulates bone tissue growth but also promotes the migration and proliferation of the vessels. Considering these features, our study further investigated the molecular biological mechanism in which OPN promotes angiogenesis in vascular endothelial cells (VECs) to find new therapeutic targets to develop pharmacological alternatives to invasive treatment methods.

2. Material and methods

2.1. Animals

All experimental protocols involving animals were approved by the Animal Ethics Committee at Anhui Medical University (License No. LLSC20221240) and are in accordance with the ARRIVE guidelines [21] and local and national legislation. Male Sprague Dawley rats aged 15–18 weeks and weighing 350–380 g were procured from the Animal Center stationed at Anhui Medical University (Hefei, Anhui, China); Male C57BL/6JNifdc mice, phenotype of the DIO (Diet-Induced Obesity) diabetes, aged between 9 and 10 weeks and weighing 24–28 g, were obtained from VITAL RIVER (Shanghai, China). All animals were accommodated within the Animal Experiment Center belonging to the School of Basic Medical Sciences of Anhui Medical University under the temperature of 20–25 °C, and a 12 h/12 h light–dark cycle.

2.2. Anesthesia

All animal experiments were carried out under anesthesia, and every effort was made to minimize the animals' pain, discomfort, and death. Prior to being anaesthetized, the animals were subjected to 8–12 h fasting. Anesthetic administration was conducted intraperitoneally, employing a concentration of 50 mg/kg [22,23] of Zoletil®50 (Virbac, France), with dosage apportioned as follows: 0.1–0.15 mL/100 g for male Sprague Dawley rats and 0.05–0.06 mL/10 g for male C57BL/6JNifdc mice. Prior to administration, the lyophilized powder was diluted with 5 mL of sterile water, yielding a solution with concentrations of 50 mg/mL tiletamine and 50 mg/mL zolazepam.

2.3. The tibial cortex transverse transport (TTT) model

Male Sprague Dawley rats were randomly assigned to three groups: Group A, the Sham group, which simulated the surgical exposure process without any fenestration or external fixation installation; Group B, the NTT (non-transverse transport) group, which simulated the physiological bone healing process and involved fenestration but no external fixation installation; and Group C, the TTT (tibial cortex transverse transport) group, which simulated the complete process of transverse bone transport involving both fenestration and external fixation installation. The external fixation was purchased from Aike Medical Equipment Co., Ltd (Shanghai, China) [16].

Surgical and bone transport process: ① Once the anesthesia took effect, the unilateral limb underwent routine disinfection and draping. ② An arcuate incision was made at the upper-middle 1/3 of the medial edge of the tibia, where the skin and subcutaneous tissue were sequentially incised, and the tissue was sharply dissected to the surface of the tibia. ③ A block of bone was prepared by using a micro-osteotomy guide plate to punch several holes along the border of the block. ④ After the transverse bone transport external fixation was installed, the bone block was completely dissociated. ⑤ The incisions were then sutured layer by layer. ⑥ For three days immediately after the operation, the incisions were cleaned daily with povidone-iodine and the rats were injected subcutaneously with 80,000 IU of veterinary penicillin sodium to prevent infection. ⑦ Beginning postoperative day 3, the bone block was transported continuously at a speed of 0.4 mm/day for 5 days, rested for 3 days while maintaining the height of traction, and then transported in the opposite direction at the same speed.

Model assessment: After operation, the operative tibial skeletal conditions of the rats in each group were explored using an X-Ray C-arm imaging system (RWD, Shenzhen, China). During bone transportation, a laser speckle perfusion imaging system (Perimed, Sweden) was used to record the local blood flows of both lower limbs at three different time points: preoperative, the fifth day of positive lifting, and the fifth day of reverse lifting. All data were normalized to the blood flow value of limbs without incisions in the sham group.

Sample collection: Under anesthesia, the tibial and surrounding tissues from the transported limbs of the rats were collected. Then, the rats are euthanized by being made to inhale high concentrations of CO_2. Samples were fixed using 4% polyformaldehyde and then sequentially subjected to decalcification (JYBL-III, LEAGENE, Beijing, China), dehydration with gradient alcohol, and paraffin embedding. The remaining para-osseous tissues were harvested, weighed, and rapidly frozen with liquid nitrogen for later use.

2.4. Immunostaining

The tissue morphology of the samples was observed using hematoxylin and eosin (H&E) staining. Paraffin tissue samples were sectioned, baked, dewaxed twice through xylene and graded ethanol to water, and then stained with eosin and hematoxylin solutions for contrasting cytoplasm and nucleic entities. Sequentially, sections were dehydrated in increasing concentrations of ethanol and xylene twice for

clearing, then embedded in neutral resin for microscopy examination. The deposition of collagen in the samples was observed using Masson's trichrome staining. The dewaxing procedure was as described above, followed by the utilization of a Masson's trichrome staining kit (B022, Ebiogo, Hefei, Anhui, China). This involved the sequential application of several solutions: light green aniline blue stain, hematoxylin stain, Beirich scarlet acid fuchsin stain, phosphomolybdic acid solution, and aniline blue stain. The samples were then progressively dehydrated with graded alcohol and two rinses of xylene before being sealed with neutral resin. Immunohistochemical methods were applied to examine the expression of angiogenic factors and target proteins within the tissue. Paraffin sections sequentially underwent baking, dewaxing, and antigen repair, followed by the application of primary antibodies – VEGF-A (vascular endothelial growth factor A) (bs-1313R, rabbit, 1:400, Bioss, Beijing, China), CD31 (sc-376764, mouse, 1:100, Santa Cruz, USA), and osteopontin (ab63856, rabbit, 1:200, Abcam, Cambridge, UK). These were detected using a polymer detection system for mouse/rabbit (B001, Ebiogo, Hefei, Anhui, China). After coloration, the sections were counterstained with hematoxylin, dehydrated, and then sealed with neutral resin. Immunofluorescence double staining was utilized to allow for the observation of the interrelationship between the key factors. Paraffin sections sequentially underwent baking, dewaxing, antigen repair, perforation, and sealing. The mixed dual-labeled antibodies (VEGF-A + Oria1/2/3 (calcium release-activated calcium modulator 1/2/3), VEGF-A + STIM1/2, CD31+Orai1, CD31+STIM1, VEGF-A + Osteopontin) were applied, which included Orai1 (28411-1-AP, rabbit, 1:200, Proteintech, Wuhan, China), Orai2 (20592-1-AP, rabbit, 1:200, Proteintech, Wuhan, China), Orai3 (25766-1-AP, rabbit, 1:200, Proteintech, Wuhan, China), STIM1 (11565-1-AP, rabbit, 1:200, Proteintech, Wuhan, China), STIM2 (21192-1-AP, rabbit, 1:200, Proteintech, Wuhan, China), VEGF-A (sc-7269, mouse, 1:100, Santa Cruz, USA), CD31 (sc-376764, mouse, 1:100, Santa Cruz, USA), and Osteopontin (ab63856, rabbit, 1:200, Abcam, Cambridge, UK). After incubating the mixed primary antibodies and washing, fluorescent secondary antibodies were added and then washed off, specifically goat anti-rabbit IgG (FITC, 1:400, B029, Ebiogo, Hefei, Anhui, China) and goat anti-mouse IgG (CY3, 1:400, B026, Ebiogo, Hefei, Anhui, China). Then, a tissue auto-fluorescence quencher (C1212, APPLYGEN, Beijing, China) was added and sealed with an anti-fluorescence quenching mounting medium with DAPI (B024, Ebiogo, Hefei, Anhui, China). The sections were scanned and pictured using a digital slide scanner (Pannoramic MIDI, 3DHISTECH, Hungary). The immuno-stained results were observed and analyzed via the Image J software (National Institutes of Health, Maryland, USA).

2.5. Laser capture microdissection (LCM) and protein profile analysis

Sample preparation: Based on the results of the fluorescent double-staining process, the regions that positively expressed VEGF-A and Orai1 in para-osseous tissues of the transport area were marked. After the paraffin tissue was sliced from the same source, it was placed on a film slice (11505151, Leica, Wetzlar, Germany) used for laser cutting. The paraffin was removed from the slices through baking, then the tissue was H&E stained. In reference to the above marked region, a laser capture microdissection system (DFC70007, Leica, Wetzlar, Germany) was used to acquire microscopic tissue samples [18]. Proteomic analysis: Preprocessing of the above tissues was carried out using the single-pot solid-phase-enhanced sample preparation (SP3) method to acquire the tissue protein-extracted solution [24]. After the addition of DTT and IAA, which was followed by centrifugation and supernatant removal, NH_4HCO_3 was added. Post-centrifugation and supernatant removal were conducted, tubes were replaced, trypsin was added, and peptide desalting was performed using a C_{18} cartridge. The peptides were freeze-dried, reconstituted with 0.1% formic acid solution, and quantified (OD at 280 nm). Samples were separated using the Nano Elute liquid phase system. In addition, mass spectrometry data identification, along with protein qualitative and quantitative analyses, were carried out using the mass spectrometer (timsTOF Pro, Thermo Scientific, Massachusetts, USA), followed by bioinformatics analysis.

2.6. Cell culture

Human umbilical vein endothelial cells (HUVEC) (Guandao Biotech, Shanghai, China) were cultured in RPMI-1640 medium (HyClone, Utah, USA) supplemented with 10% fetal bovine serum (BC-SE-FBS01, Biochannel, Nanjing, China), 100 U/mL penicillin G, and 100 U/mL streptomycin sulfate (91670249, YEASEN, Shanghai, China). The cells were incubated at 37 °C in a culture chamber with 5% CO_2 concentration. For the protein stimulation group, purified osteopontin (OPN) (human source, HY-P70499, MCE, New Jersey, USA) was used.

2.7. RNA interference

OPN siRNA was transfected into HUVEC cells through lipid-mediated transfection. The OPN siRNA and scrambled siRNA were synthesized by GENERAL BIOL (Anhui, China), and their sequences are shown in (Table 1). Initially, the OPN siRNA and Lipo3000 (L3000-015, Invitrogen, California, USA) were diluted separately using Opti-MEM (3198–5070, Thermo, Massachusetts, USA). The diluted solutions were then mixed to form a transfection compound, which was combined with the complete culture medium being added to the cells and incubated at a constant temperature in an incubator for subsequent experiments.

2.8. Quantitative real-time PCR (qPCR)

The cell samples were added with Trizol reagent (DP424, TIANGEN, Beijing, China), followed by chloroform centrifugation. The supernatant collected was added to isopropanol and centrifuged again. The precipitate, after being washed with 75% ethanol, was dissolved in DEPC water (10601ES76, YEASEN, Shanghai, China) to prepare the total RNA. Using HiScript II qRT SuperMix II (R223-01, Vazyme, Nanjing, China) and a PCR machine (TC-96, Bioer Technology, Hangzhou, China), total RNA was reversely transcribed to obtain cDNA.

The primers used for qPCR were synthesized using GENERAL BIOL (Anhui, China). The primer sequence information is provided in (Table 2). The materials were added in sequence to the ice—cDNA template, upstream and downstream primers, Hieff UNICON® Universal Blue qPCR SYBR Green Master Mix (11184 ES, YEASEN, Shanghai, China), and RNase-Free ddH_2O. Two-step amplification was performed (95 °C for 2 min; 95 °C for 10 s, 60 °C for 30 s, 40 cycles; 95 °C for 1 min, 60 °C for 15 s, 98 °C for 5 s).

2.9. Cellular migration and proliferation

A horizontal line was drawn on the reverse side of a 12-well plate, positioning the pipette tip perpendicular to the scratch. The cells scratched away were rinsed off with PBS (G4202, Servicebio, Wuhan, Hubei, China), followed by the addition of a serum-free medium. Subsequently, the area of the scratch at the 0-h checkpoint was photographed for reference. After the completion of 24 h of incubating, the current scratch area was again photographed. The wound closure ratio = (area at 0 h – area at 24-h)/area at 0 h.

After pre-incubation for 4 h, CCK-8 solution (40203ES76, YEASEN,

Table 1
siRNA sequences for target genes.

Target	Sequence
OPN siRNA	Sense: 5'-GGG AAG GAC AGU UAU GAA ATT-3'
	Antisense: 5'-UUU CAU AAC UGU CCU UCC CTT-3'
Scrambled siRNA	Sense: 5'-UUC UCC GAA CGU GUC ACG UTT-3'
	Antisense: 5'-ACG UGA CAC GUU CGG AGA ATT-3'

Table 2
Primer sequences for target genes.

Gene	Sequence
OPN	Sense: 5'- CTC CAT TGA CTC GAA CGA CTC -3' Antisense: 5'- CAG GTC TGC GAA ACT TCT TAG AT -3'
GAPDH	Sense: 5'-ACC CAG AAG ACT GTG GAT GG -3' Antisense: 5'-TGA GCT TGA CAA AGT GGT CG-3'

Shanghai, China) was added into the 96-well plates and then incubated for another 4 h. An absorbance at 450 nm was determined using a microplate reader (KC-100, Caretiun, Shenzhen, China).

2.10. Angiogenesis

On the day prior to the experiment, matrigel (354248, Corning, USA) was slowly thawed overnight at 4 °C then diluted with identical volume of complete culture medium in pre-chilled centrifuge tubes and added to the 96-well plates. The plates were then kept in a 37 °C incubator for 1 h. Cells from different groups were enzymatically digested using trypsin, resuspended in a complete 1640 medium for counting, and finally incubated in the matrigel-coated plates with a density of 30,000 cells per well. After 4 h of incubation, cell images were captured under a microscope.

2.11. ELISA assay

The concentrations of endothelial nitric oxide synthase (eNOS) and nitric oxide (NO) in the para-osseous tissues were measured using the endothelial nitric oxide synthase ELISA kit (JYM0338Ra & 20220510, ELISA LAB, Wuhan, China) and the nitric oxide ELISA kit (A015-2-1 & 20220316, Jiancheng, Nanjing, China). The levels of eNOS and NO within cells were quantified using a human endothelial nitric oxide synthase ELISA Kit (ml025093, mlbio, Shanghai, China) and griess reagent I and II (YT286, Biorab, Beijing, China).

2.12. Western blotting

Cells were lysed on ice with RIPA buffer (P0013B, Beyotime, Shanghai, China), and the supernatant was collected after centrifugation. Then, 10% SDS-PAGE gel electrophoresis was carried out, followed by being transferred to a PVDF membrane. After a 2-h block in a western blotting buffer (5% non-fat milk), the membrane was incubated overnight in a shaker with primary antibody dilution. The primary antibodies used specifically were OPN (bs-23258R, rabbit, 1:1000, Bioss, Beijing, China; ab63856, rabbit, 1:1000, Abcam, Cambridge, UK), Orai1 (ab111960, rabbit, 1:1000, Abcam, Cambridge, UK; 28411-1-AP, rabbit, 1:500, Proteintech, Wuhan, China), STIM1 (11565-1-AP, rabbit, 1:1000, Proteintech, Wuhan, China), eNOS (bs-20608R, rabbit, 1:1000, Bioss, Beijing, China), p-eNOS (bs-3589R, rabbit, 1:1000, Bioss, Beijing, China), and GAPDH (TA-08, mouse, 1:2000, Zsbio, Beijing, China). Afterward, HRP-conjugated secondary antibodies were diluted in a secondary antibody dilution solution, specifically goat anti-rabbit (ZB-2301, Zsbio, Beijing, China) and goat anti-mouse (ZB-2305, Zsbio, Beijing, China) at a ratio of 1:20000. After 2 h of incubation at room temperature, an ECL detection kit (340958, Thermo, Massachusetts, USA) was used to detect the proteins. The density quantification of the immunoblot was carried out with a chemiluminescent gel imaging analysis system (Bio-Rad, California, USA).

2.13. Calcium imaging

Different groups of cell cultures were first incubated with a solution of the calcium ion fluorescent probe Fura-8/AM (ab142773, Abcam, Cambridge, UK) for 30 min, then washed with an Ca^{2+}-free physiological saline solution (OPSS) (140 mmol/L NaCl, 5 mmol/L KCl, 2 mmol/L $MgCl_2$, 10 mmol/L glucose, 0.2 mmol/L EGTA and 10 mmol/L HEPES, pH = 7.4) and placed in the bath of a calcium imaging system. 50 μL of 2 mmol/L thapsigargin (TG) (T7459, Thermo, Massachusetts, USA) was added. After the fluorescence intensity stabilized, the supernatant was removed and replaced with a 50 μL of 2 mmol/L Ca^{2+} solution. The concentration changes of intracellular calcium ions were calculated based on the ratio of the fluorescence intensity (F_1) after calcium was added to the baseline fluorescence intensity (F_0) before TG addition (F_1/F_0).

2.14. Wound healing on the skin of diabetic mice

Diabetes mice with diet-induced obesity (DIO) [25] were randomly divided into three groups according to different injected drugs. Group A was the PBS group; the mice here were injected with PBS. Group B was the standard dosage group of OPN, and the mice in this group were injected with OPN (of mouse origin, ab281820, Abcam, Cambridge, UK) at a concentration of 1 μg/mL. Group C was the high-dosage OPN group—mice in this group were injected with homotypic OPN at a concentration of 10 μg/mL. All the mice were acclimatized in a clean-grade animal experimental center for seven days, during which they were consistently fed a high-fat diet. The fasting blood glucose levels and body weight of the mice were diligently documented at three distinct time intervals (i.e., one day, three days, and seven days post-admission into the center). Once satisfactory anesthesia levels were achieved in the mice, the hair on their backs was shaved off. Following routine disinfection, 5 mm-circular-skin-wound were made using a skin punch device. As per the pre-surgery groupings, the above-mentioned medicines were then injected into the wound and around it, with reference to the multi-point subcutaneous injection method of OPN around the wound surface by Tanaka S [26]. The total injection dosage was 1 mL, divided over two days. Post-injection, the wound was covered with Vaseline gauze. Photographic documentation of wound healing was carried out on postoperative days 0, 1, 5, 9, and 12. On the 5th and 12th days, skin tissue samples were collected under anesthesia, and the samples were preserved with 4% polyformaldehyde. Finally, the mice were euthanized by inhaling high concentrations of CO_2.

2.15. Statistical analysis

Image analysis was conducted using Image J software (National Institutes of Health, Maryland, USA). All data is presented as mean ± S.E.M., and analyzed using GraphPad Prism version 8.0.2.263 (San Diego, California, USA). To compare the two groups, Student's *t*-test (independent samples) was employed. For comparing more than two groups, one-way analysis of variance (ANOVA) complemented by Welch's multiple comparisons test was used to determine statistical significance. For all the statistical analyses, when $p < 0.05$, differences were considered statistically significant.

3. Results

3.1. Increase in local blood flow in the surrounding area of transverse transport bone obviously increased

To explore the molecular biological mechanism of bone-transverse-transporting-improved local blood flow, we reproduced the manipulation process on rats by installing a micro-transverse bone-transporting fixed stand [16], as shown in (Fig. 1A). With the help of an X-ray C-arm imaging system, the conditions of the modeled rats in each group were evaluated (Fig. 1B); it was found that all the tibial tissue could satisfy the requirement. Meanwhile, during the entire transporting period, the laser speckle perfusion imaging system was used to monitor the local blood flow changes in the dual sides of the lower limbs [27]. The results presented in (Fig. 1C) show that the local blood flow in the surrounding area of tibial cortex transverse transport (TTT) clearly increased because

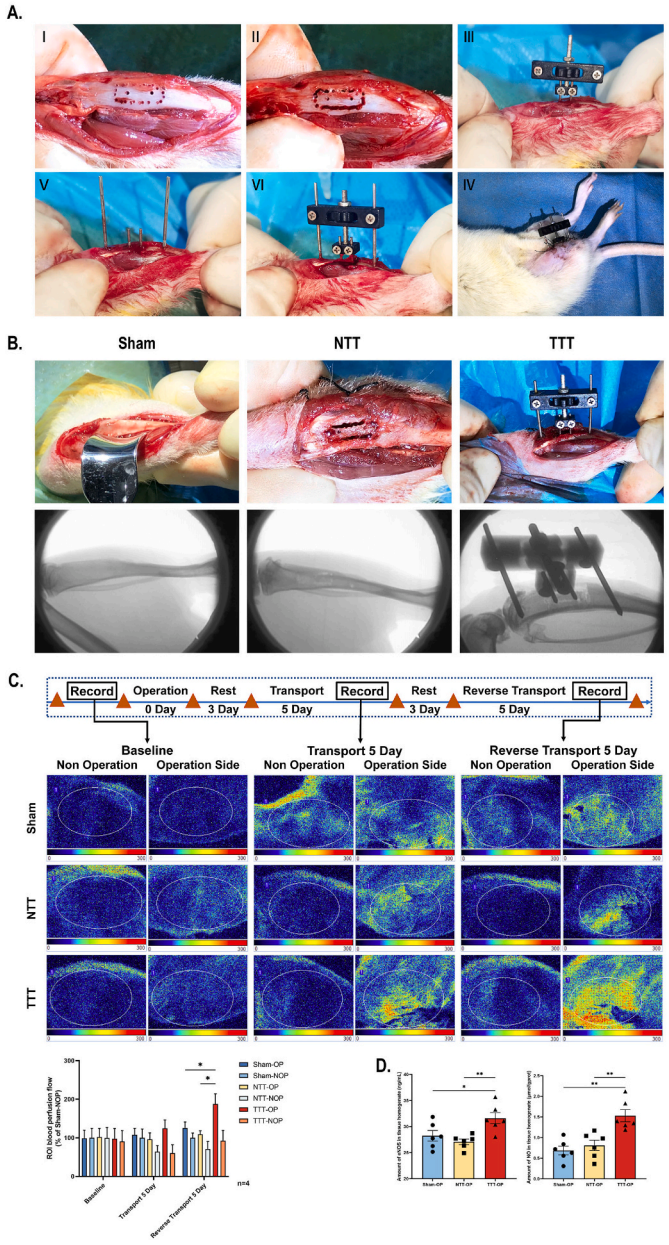

Fig. 1. The volume of local blood flow around transverse transport bone showed an obvious increase. (A) The whole surgical procedure of rat tibial cortex transverse transport (TTT) model establishment by stalling the micro-transverse bone transport fixing stand. (B) X-ray images of rats' tibias belonging to different groups. NTT is short for non-transverse transport, and TTT is short for tibial cortex transverse transport. (C) The time axis of the process of TTT and the blood flow changes around the dual limbs of rats at each time point, containing pre-surgery, the fifth day of the bone block transported period, and the fifth day of the reverse-transported period. n = 4. All the flow volumes were normalized to those of the non-surgery limb of the sham group. (D) Endothelial nitric oxide synthase (eNOS) and nitric oxide (NO) contents within the region around the transport area were detected by ELISA assay. n = 6. All the data in the bar graph is presented as mean ± S.E.M., which $*p < 0.05$ and $**p < 0.01$.

the blood flow surrounding the rats' tibias in the TTT group showed statistically significant differences compared to the other groups ($*p < 0.05$). In addition, the results of the ELISA assay indicated that the content of either endothelial nitric oxide synthase (eNOS) or nitric oxide (NO) of the TTT group was greater than that of the other groups (Fig. 1D), which indicated statistically significant differences ($*p < 0.05$, $**p < 0.01$). The above in vivo observation confirmed the effect of TTT-increased local blood flows.

3.2. Expression of Orai1/STIM1 on the para-osseous tissues of the transport area

When analyzing the para-osseous tissues of the transport area near the tibia using immunohistochemistry, we found that vascular endothelial growth factor A (VEGF-A) and platelet endothelial cell adhesion molecule CD31 were both expressed, implying that the growth of vascular tissue accompanied the healing process (Fig. 2A). Considering that the healing process of bone tissue is involved in the recruitment of calcium, we first planned to verify the activated situation of store-operated calcium entry (SOCE) and determine which subtype of calcium channel is highly expressed [28]. Specifically, we detected the co-expression of VEGF-A and each subtype of calcium release-activated calcium modulator (Orai), Orai1/2/3, or each subtype of stromal interaction molecule (STIM), STIM1/2, on the tissue of the TTT group. As shown in (Fig. 2B), among several subtypes, Orai1/STIM1 displayed apparent expression in the TTT group, exhibiting statistically significant differences ($*p < 0.05$). Through the semiquantitative western blotting analysis (Fig. 2C), it was found that Orai1, STIM1, and phosphorylated eNOS (p-eNOS) expressed significantly increased in the group of TTT group compared to that of the others group ($*p < 0.05$, $**p < 0.01$, $***p < 0.001$). Meanwhile, there was a statistically significant difference in p-eNOS/eNOS between the TTT and Sham group ($*p < 0.05$) indicating the obvious activation of eNOS in the TTT group. However, there existed no significant statistical difference among groups' eNOS. Further analysis of the dual staining of VEGF-A/CD31 and Orai1/STIM1 (see in Fig. 2D–E) showed higher levels of expression in the para-osseous tissues of the transport area of the TTT group compared to the other groups, exhibiting statistically significant differences ($*p < 0.05$, $**p < 0.01$, $***p < 0.001$). Combined with the results about eNOS and NO in Section 3.1, these findings suggest that during the process of TTT, SOCE is activated, which elevates the activity of eNOS, thereby promoting the release of NO and increasing local blood flow.

3.3. Osteopontin-expressed enhancement on the para-osseous tissues of the transport area

To the best of our knowledge, no report about the relationship between bone transport and SOCE has been found. Therefore, we chose to determine whether the area in both VEGF-A and Orai1 were positively expressed to explore whether bone transport relates to SOCE. We utilized the method of laser capture microdissection (LCM) to orientationally cut the dual-positive region within the para-osseous tissues of the transport area in the TTT group and the same region near the tibia in the NTT group (Fig. 3A), followed by the proteomic analysis. As shown in (Fig. 3C), the result of the proteomic analysis showed that 39 kinds of protein were detected in the sample of the TTT group, among which 15 kinds of protein could also be detected in the sample of the NTT group, while the other 24 kinds of protein were detected only in the sample of the TTT group. A gene ontology (GO) analysis of these 39 proteins found that they mainly enriched in the developmental process, locomotion, and cellular process (Fig. 3B). Further analysis of protein–protein interaction networks (PPI) as regards the expressed proteins detected in the TTT group showed that osteopontin (OPN), which only appeared in the TTT group, was located in the center of the protein network (Fig, 3D), supporting Dai J et al.'s finding that OPN could improve angiogenesis [20,29,30]. Through the semiquantitative western blotting analysis (Fig. 3E), it was found that OPN expressed significantly increased in the TTT group compared to that of the NTT group ($***p < 0.001$). This result confirmed that TTT could induce the increase of expression of OPN. Subsequently, we applied immunohistochemistry and immunofluorescence double staining of VEGF-A and OPN to confirm the highly expressed condition of OPN on the para-osseous tissues

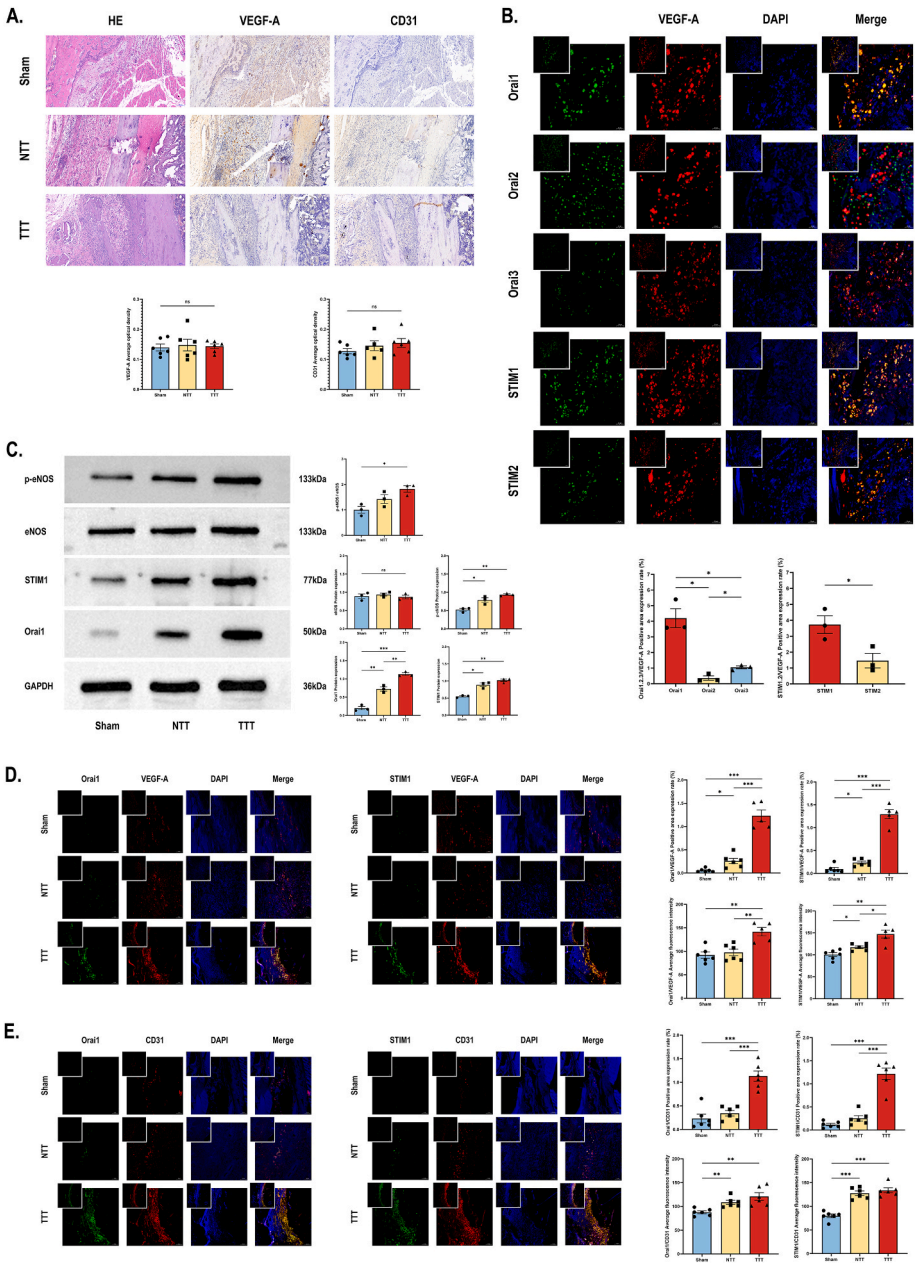

Fig. 2. The expression of Orai1/STIM1 on the para-osseous tissues of the TTT group increased in a large number. (A) Double immunostaining of VEGF-A and CD31 on the para-osseous tissues showing the new-grown vessels. The magnification is 100 ×. Except for the number of samples in the NTT group used for CD31 staining, which is 5, the number of samples in other groups is 6. (B) Double immunostaining of VEGF-A (shown in red) and each subtype of calcium release-activated calcium modulator (Orai), Orai1/2/3 (shown in green), or each subtype of stromal interaction molecule (STIM), STIM1/2 (shown in green) on the para-osseous tissues of the TTT group. The magnification is 400 ×. n = 3. DAPI represents the cellular nuclei, shown in blue. Statistical results were presented as the rate of the area of positive dual-staining signal to the area of the positive signal in single channel of red. (C) The expression level of p-eNOS, eNOS, Orai1 and STIM1 in each group was detected by western blotting. The right chart shows the gray scale statistics including showing the ratio of p-eNOS and eNOS. n = 3. (D) Double immunostaining of VEGF-A (shown in red) and Orai1 (shown in green) or STIM1 (shown in green) on the para-osseous tissues of each group. The magnification is 200 ×. Except for the number of samples in the TTT group, which is 5, the number of samples in the other groups is 6. (E) Double immunostaining of CD31 (shown in red) and Orai1 (shown in green) or STIM1 (shown in green) on the para-osseous tissues of each group. The magnification is 200 ×. n = 6. All the data in the bar graph is presented as mean ± S.E.M. *$p < 0.05$, **$p < 0.01$, and ***$p < 0.001$. (For interpretation of the references to color in this figure legend, the reader is referred to the Web version of this article.)

(Fig. 3F–G). Binding with the expressed condition of SOCE members Orai1 and STIM1 and the contents of eNOS and NO within the para-osseous tissues, it is implied that OPN might activate Orai1/STIM1 to exert the pro-angiogenesis effect in the TTT process.

3.4. OPN's promotion of the migration, proliferation, and angiogenesis of vascular endothelial cells; the release of NO by eNOS, and the activation of soce

To ascertain the influence of OPN on VECs, we tested the functional changes of human umbilical vein endothelial cells (HUVEC) stimulated by purified OPN, setting three concentrations graded 0.5, 0.7, and 1.0

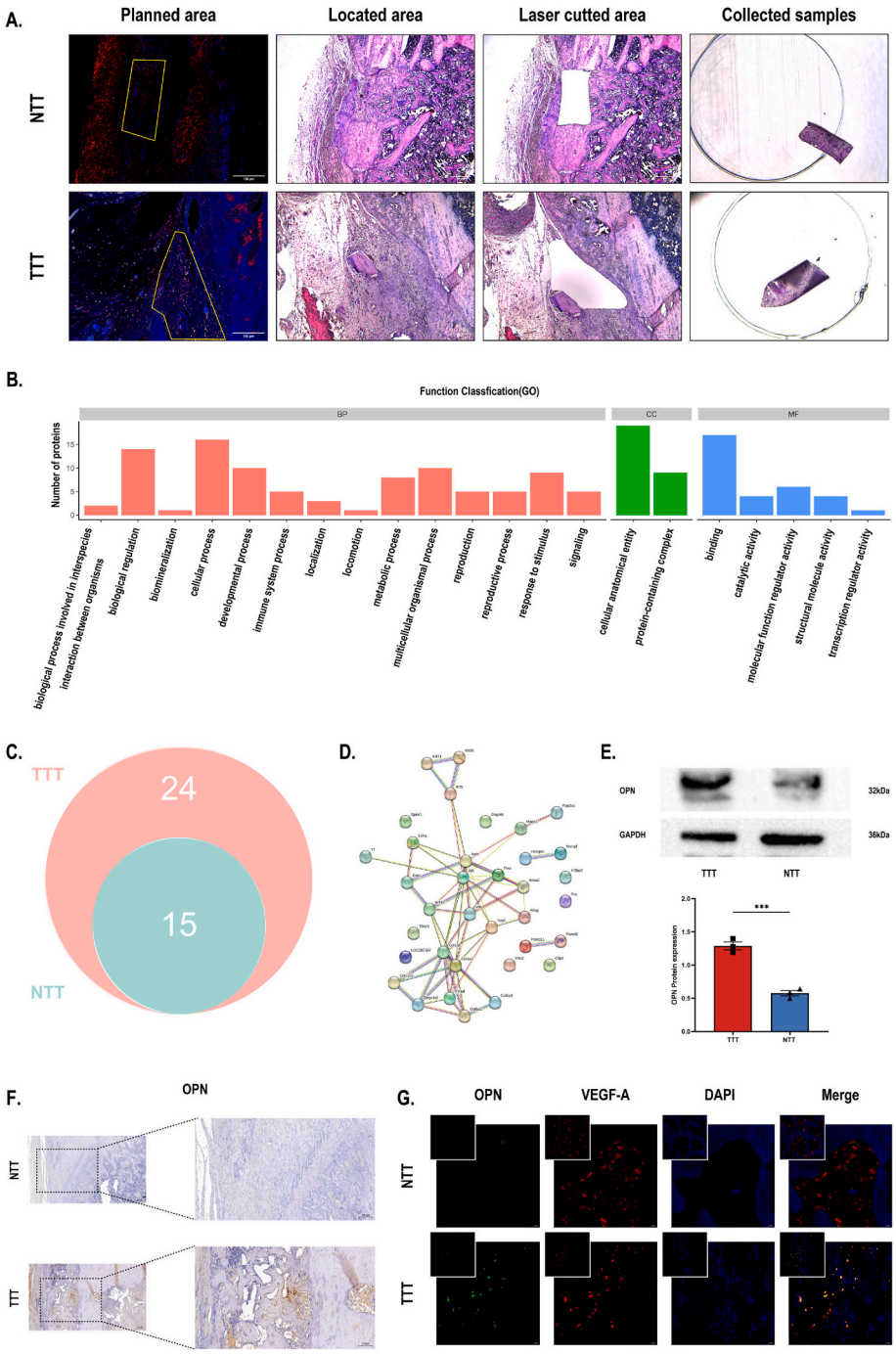

Fig. 3. Osteopontin (OPN) on the para-osseous tissues of the TTT group was significantly enhanced. (A) Based on the positive dual-staining area of VEGF-A and Orai1 (shown at a magnification of 100 ×), tissues within the planned area were acquired by utilizing laser capture microdissection (LCM). (B) Gene ontology (GO) analysis of the proteins discovered by proteomics. (C) The Venn diagram presents the distinct expression profiles of the TTT and NTT groups. (D) The protein–protein interaction networks (PPI) analysis of the expressed in the TTT group indicated their functional relationship. (E) The expression level of OPN in each group was detected by western blotting. The right chart shows the gray scale statistics. n = 3. (F) Immunohistochemical staining of the para-osseous tissues of the NTT and the TTT groups detected the expression of OPN, shown at a magnification of 100 ×. (G) Double immunostaining of VEGF-A (shown in red) and OPN (shown in green) or STIM1 (shown in green) on the para-osseous tissues of each group. The magnification is 400 ×. DAPI (blue) presents the cellular nuclei. n = 5. (For interpretation of the references to color in this figure legend, the reader is referred to the Web version of this article.)

μg/mL by referring to the study of Rotem I et al. [31,32] and three incubated time periods of 12, 24, and 48 h. According to the results shown in (Fig. 4A), treatment for 12 h or 48 h at 0.7 or 1.0 μg/mL of OPN remarkably improved the pro-healing of the scratch and proliferation of HUVEC compared to the control group (*$p < 0.05$, **$p < 0.01$ and ***$p < 0.001$); all the three concentrations of OPN treated for 24 h could significantly improve cellular migration and proliferation with statistical significance (*$p < 0.05$, **$p < 0.01$ and ***$p < 0.001$). Taking these results together, we chose to stimulate the cells 24 h by OPN at 1.0 μg/mL in the subsequent experiments. On the other hand, in the OPN group's knockdown through siRNA transfection (Fig. 4B), the cellular function of migration and proliferation was significantly inhibited compared to that of the group transfected with scrambled siRNA (*$p <$ 0.05 and ***$p < 0.001$) (Fig. 4C). These results verified the notion that

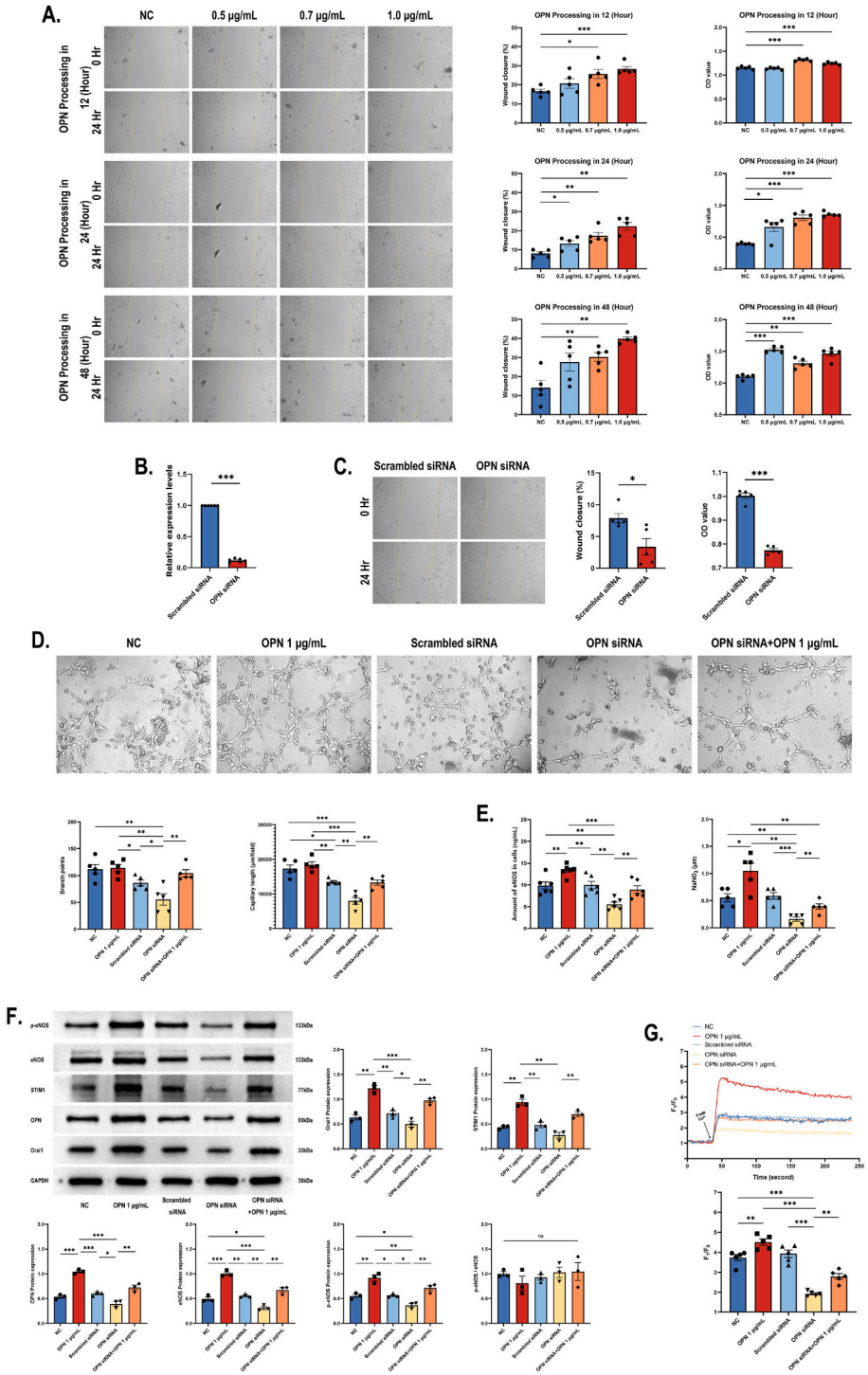

Fig. 4. OPN could improve the migration, proliferation, and angiogenesis of HUVECs as well as the activation of SOCE, eNOS, and NO release. (A) Stimulation by purified OPN, setting three concentrations graded 0.5, 0.7, and 1.0 μg/mL at three incubated time periods of 12, 24, and 48 h, showed dose- and time-dependent influence on the scratch closure of human umbilical vein endothelial cells (HUVEC) after 24 h. The photographs were shown at a magnification of 40 ×. The statistical analysis indicated the cellular migration function. A CCK-8 assay was used to evaluate the proliferation function of cells. n = 5. (B) The interference of OPN was verified by a qPCR experiment. n = 6. (C) Migration and proliferation functional changes of OPN-siRNA-treated HUVECs. The magnification is 40 ×. n = 5. (D) On the basis of the division of groups in the experiment of migration, another group of OPN-knockdown cells stimulated by OPN was added. Then, the function of HUVECs' angiogenesis in every group was observed. The magnification is 40 ×. n = 5. (E) Measurement of eNOS (n = 6) and NO (n = 5) in each group by ELISA. (F) The expression level of OPN, Orai1, STIM1, eNOS, and p-eNOS in each group was detected by western blotting. The right chart shows the gray scale statistics including the ratio of p-eNOS and eNOS. n = 3. (G) The fluorescence changes of intracellular and extracellular calcium ions in five groups of cells were recorded using a calcium imaging system. F_1 is the fluorescence intensity after calcium was added, and F_0 is the baseline fluorescence intensity. All the data in the bar graph is presented as mean ± S.E.M. $^*p < 0.05$, $^{**}p < 0.01$ and $^{***}p < 0.001$.

OPN is involved in the regulation of HUVEC migration and proliferation.

In the experiment of vascular formation, we aim to further explore whether exogenous supplemented OPN could rescue the deficiency of vascular formation in HUVECs. We added a group of OPN-interfered cells stimulated by purified OPN. The results indicated that supplying purified OPN to the OPN-knockdown cells' patent enhancement of angiogenetic functions (**$p < 0.01$) (Fig. 4D). Then, when detecting the released content of eNOS and NO by ELISA, it was found that either direct application of OPN or re-supplementing OPN after interference could effectively prompt eNOS in HUVEC to produce more NO (Fig. 4E), existing statistical significance (**$p < 0.01$ and ***$p < 0.001$).

Through the semiquantitative western blotting analysis (Fig. 4F), it was found that Orai1, STIM1, eNOS, and p-eNOS expressed significantly increased in the group of OPN-stimulation or OPN siRNA added with OPN compared to that of the control group (**$p < 0.01$ and ***$p < 0.001$). These results confirmed that OPN could increase the expression of Orai1, STIM1, eNOS, and p-eNOS. However, there existed no significant statistical difference among groups' p-eNOS/eNOS.

The next work focused on the relationship between OPN and SOCE. Under the monitoring of the calcium imaging system, the calcium stored

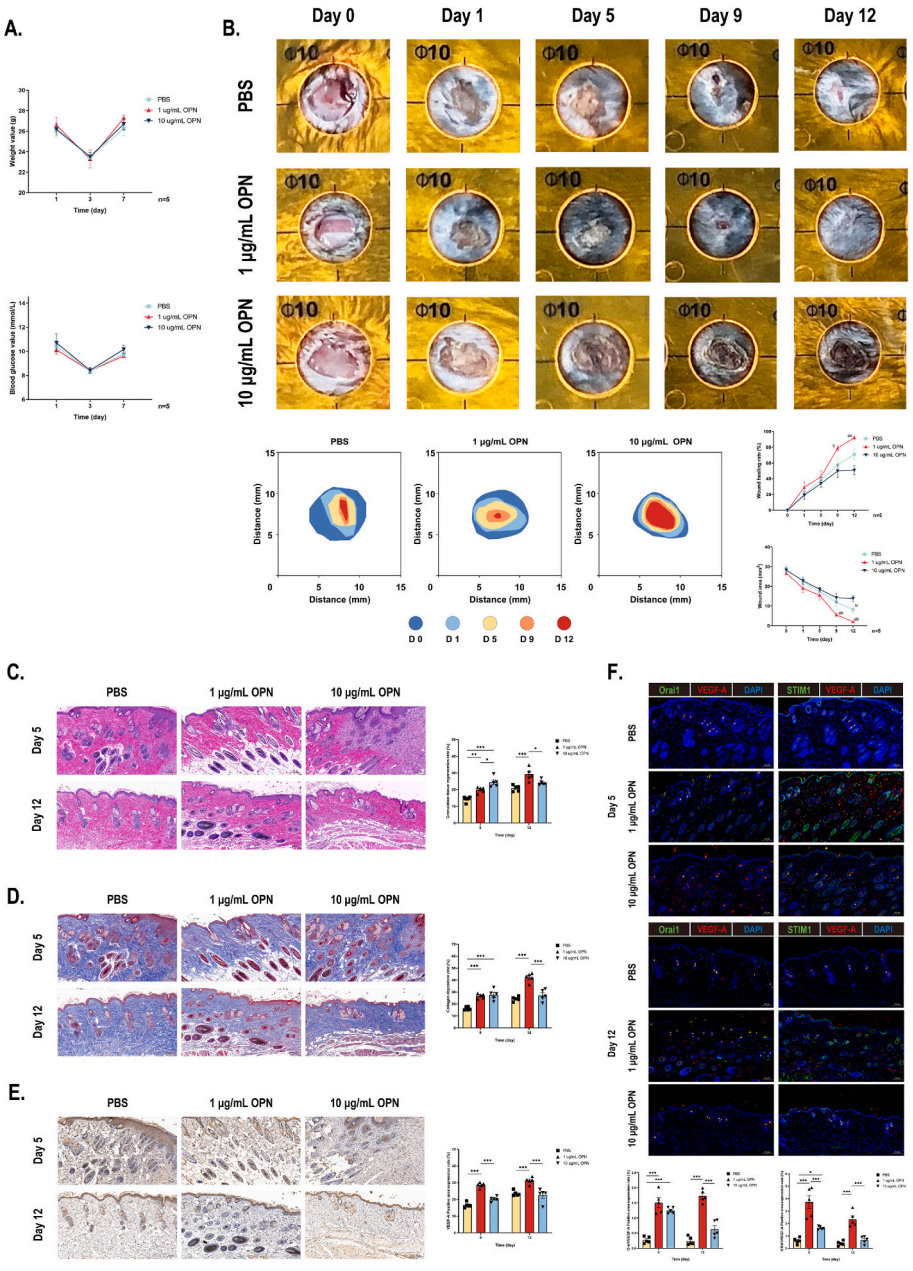

Fig. 5. OPN accelerated the healing, formation of granulation tissue, local collagen deposition, and vascular formation on wounds on the surface of diabetic mice's skin while involving activating SOCE. (A) Recording of fasting blood glucose and weight changes of the diabetic-modeled mice. (B) Photographs recording the situation of wound closure at 0–12 days post-modeling, while the stacked plots were used to display the healing process. Statistics of the wound healing rate and wound area. [a]*$p < 0.05$ vs. the PBS-treated group; [b]*$p < 0.05$ vs. the high-dose (10 μg/mL) OPN-treated group. (C) On the 5th- or 12th-day post-surgery, the formation of granulation tissue was observed by the HE-stained method. (D) On the 5th or 12th day post-surgery, the collagen deposition was observed using the Masson-stained method. (E) Immunohistochemistry testing the expression of VEGF-A on the surface of wounded skin on the 5th or 12th day post-surgery. (F) Dual-marked immunofluorescence detection of VEGF-A (red) and Oria1 (green) or STIM1 (green) on the 5th or 12th day post-surgery. All the magnifications are 100 ×. n = 5. All the data in the bar graph is presented as mean ± S.E.M. *$p < 0.05$, **$p < 0.01$ and ***$p < 0.001$. (For interpretation of the references to color in this figure legend, the reader is referred to the Web version of this article.)

in the endoplasmic reticulum was emptied by adding thapsigargin (TG), then supplied extracellular Ca^{2+}, the results showed that the ratio of post-to-baseline fluorescence intensity (F_1/F_0) of cells that were pre-treated with OPN apparently increased when compared with the control group (**$p < 0.01$) (Fig, 4G). This result could indicate that OPN regulated the increase of SOCE-mediated calcium influx. Combined with the above results about the changes of Orai1, STIM1, eNOS, and NO, it was summarized that OPN could activate the SOCE pathway to regulate the entry of extracellular Ca^{2+}, thereby improving the activation of eNOS and release of NO.

3.5. OPN activates SOCE and promotes the healing, formation of granulation tissue, local collagen deposition, and vascular formation on the skin wound surface of diabetic mice

The fasting blood glucose of the diabetic-modeled mice induced by high-fat food was severely elevated, which was more than 9.0 mmol/L and the average blood glucose value was 10.4 mmol/L (Fig. 5A), achieving the diagnostic criteria of type II diabetes [25,33]. Moreover, the changing trends of descending weight and decreasing fasting blood glucose were in the same direction (see Fig. 5A), which also conformed to the situation in which the patients with type II diabetes [34]; while the weight elevated up once again could increase sharply fasting blood glucose due to the relative insufficient of insulin release.

On the aspect of wound healing, a general comparison of the wound closure rate and unhealing area in the mice of three groups revealed that 1 μg/mL-OPN injection group displayed faster speed in healing than that of the other two groups (Fig. 5B). Specifically, in the ninth and 12th post-model-established day, the wound healing rate of the OPN-treated group marked significant gaps among the remaining two groups (*$p < 0.05$) (Fig. 5B). Conversely, a high concentration of OPN (10 μg/mL) brought delayed healing in the late period, resulting in a greater unhealed area than the PBS-treated group on the 12th day (*$p < 0.05$). All these results indicated that OPN could improve the healing of skin wounds derived from diabetes within a certain dosage range.

In the observation of the forms of wound tissues (Fig. 5C-D), we found that on the 5th-day post-surgery, either the formation of granulation tissue or the local collagen deposition of the OPN-injected group increased more than that of the PBS-injected group (**$p < 0.01$ and ***$p < 0.001$). Especially, in the high-concentration OPN (10 μg/mL) group, the formation of granulation tissue was more severe than in the other two groups (*$p < 0.05$ and ***$p < 0.001$), supporting the evidence that hyperproliferative granulation tissue is unbeneficial to the normal healing process [35,36], which was consistent with the phenomenon of high-concentration OPN delayed wound healing. On the 12th day after surgery, 1 μg/mL of OPN injection showed superior performance on the aspects of granulation formation or local collagen deposition to the other two groups (*$p < 0.05$ and ***$p < 0.001$) (Fig. 5C–D). Administration of 1 μg/mL OPN also showed excellent effect on the pro-formation of vessels on the 5th and 12th day based on the observation of higher VEGF-A expression (***$p < 0.001$) (Fig. 5E).

Further detection was conducted on the wound surface tissues by fluorescent co-staining of VEGF-A and Orai1 or STIM1, finding that five days after model establishment, the local injection of OPN could excite the co-expression of VEGF-A, Orai1, and STIM1 over that of the PBS-treated group (*$p < 0.05$、***$p < 0.001$). As shown in (Fig. 5F), the fluorescence intensity of VEGF-A merged STIM1 in the low-dose OPN (1 μg/mL) group was statistically significantly higher than that in the high-dose OPN (10 μg/mL) group (***$p < 0.001$) on the fifth day; while on the 12th day, the fluorescence intensity of VEGF-A merged STIM1 moderately descended compared to that on the fifth day, but still maintained statistical significance compared to the other two groups (***$p < 0.001$). Taken together, in vitro cellular functional assays indicated that OPN could activate Orai1/STIM1 to a certain degree, and then increase the activity of eNOS to release more NO, taking a role in vascular vasodilation leading to increasing the local blood flow and promoting vascular proliferation.

In summary, in the pathophysiological process of TTT, OPN exists, which activates the Orai1/STIM1-mediated SOCE pathway. Specifically, extracellular calcium enters VECs to induce NO release enhancement induced by eNOS activation, accompanied by the release of pro-angiogenesis factor VEGF, and then increases the migration, proliferation, and angiogenesis of VECs. Improving the function of VECs to increase the local volume of blood flow finally produces the effect of improving local vessels' growth and proliferation. In vivo functional experimental verification indicates that OPN activates SOCE and promotes the healing of the skin wound surface of diabetic mice (shown in the schematical Fig. 6).

4. Discussion

In this study, we reproduced the entire operation process of tibial cortex transverse transport (TTT) in rats' lower limbs, referring to the TTT animal model developed by Yang Y [16]. A laser speckle blood flow video monitoring system was employed to confirm the increased blood flow around the transport area. Firstly, this study was the first to detect an elevated expression of Orai1/STIM1 in the tissues surrounding the bone transport area in rats, indicating the SOCE involved in the process of TTT. Secondly, we utilized laser capture microdissection (LCM) technology [18,24] for the first time to precisely cut the Orai1/STIM1-expressed areas from paraffin-embedded tissues in order to obtain microsamples for proteomic analysis. Thirdly, osteopontin (OPN) was first explored which was highly expressed in that area revealed by the results of the proteomic analysis. Additionally, the effect of OPN on promoting the proliferation, migration, and angiogenesis of VECs was confirmed. At last, we preliminarily discovered the therapeutic effect of OPN on wound healing and proposed a new mechanism mediated by SOCE. As a novel surgical approach, the TTT method is mainly employed to treat distal limb ischemia typified by diabetic foot. Research into diabetic foot has revealed [8–11] that is causes widespread endothelial cell damage in patients, leading to localized vascular constriction, diminished elasticity, and, subsequently, insufficient local blood vessels. The TTT technique, through sustained tension [12–14], promotes local cellular metabolism and hastens tissue repair and regeneration in the surgical area. Clinical case studies of patients who underwent this treatment evidenced the recanalization of occluded local vessels and microvascular proliferation [9,10,12]. Relevant foundational research also suggested that this technique could spur the regeneration of local capillary networks. Meanwhile, the expression of varieties of pro-angiogenesis molecules in the tissues surrounding the bone transport area, including vascular endothelial growth factor (VEGF), showed a significant increase [8]. However, the physiological mechanism that drives vascular proliferation has yet to be fully elucidated.

The core mechanism involved lies in the healing process of bone tissue on the cortical bone, where calcium mobilization plays a pivotal role. Porto Ribeiro T and others found [37,38] that Ca^{2+}, as a secondary messenger, enters into cells increasingly and enhances the activity of endothelial nitric oxide synthase (eNOS), under which nitric oxide synthase (NOS) catalyzes arginine to produce nitric oxide (NO). As an important intracellular signaling messenger essential for regulating vascular growth and remodeling, NO can effectively enhance the relaxation function of vascular smooth muscle and improve local microcirculation [39]. However, suppression of eNOS and NO expression occurs in the diabetic foot due to hyperglycemia-induced damage to the body's endothelial functions. An increase in the expression of eNOS and NO was detected in the tissues surrounding the bone transport area, possibly accounting for one of its efficacies in the treatment of diabetic foot [40,41]. Among the various channels that can cause extracellular Ca^{2+} influx, store-operated calcium entry (SOCE) is an important pathway that regulates intracellular calcium ion concentrations. After the Ca^{2+} stored in the endoplasmic reticulum (ER) is depleted, the

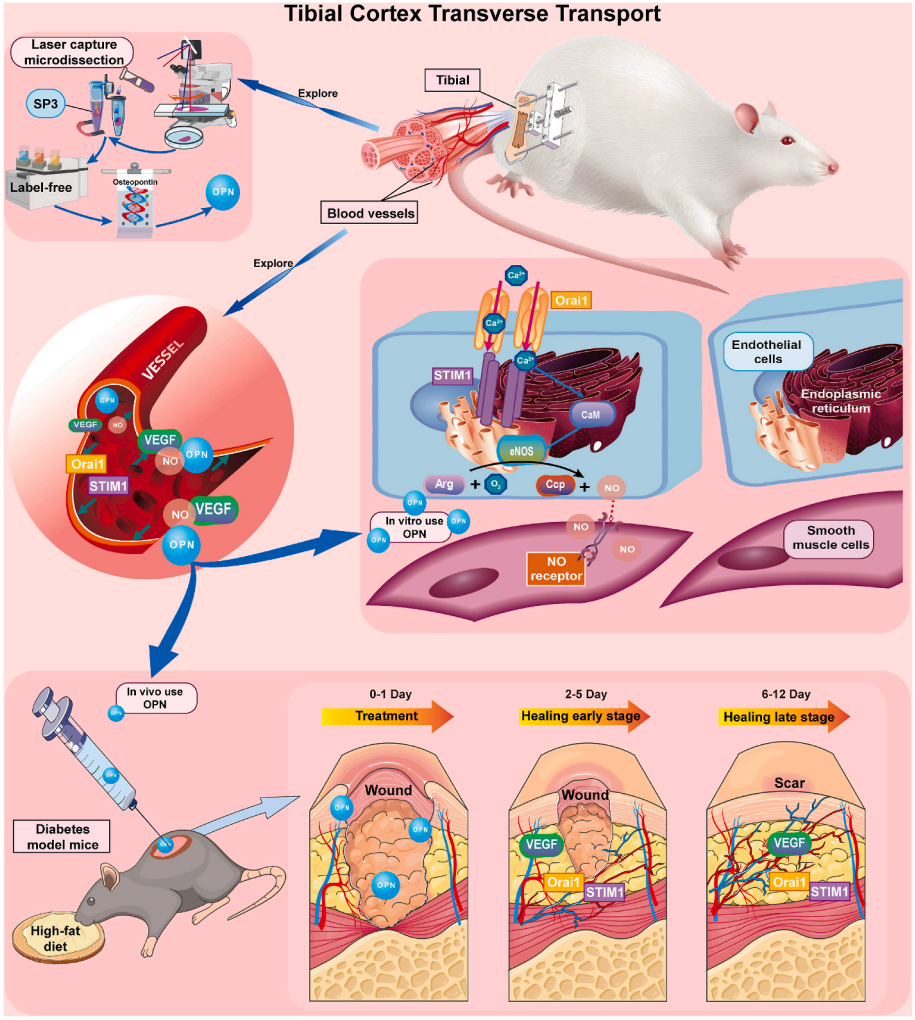

Fig. 6. The schematical figure shows the pathophysiological changes and molecular mechanisms of OPN-activated Orai1/STIM1-mediated SOCE during the TTT process. First, VEGF-A, OPN, and NO could be detected in the para-osseous tissues around the bone transport area. By acquiring the Orai1/STIM1-high-expressed tissue in the paraffin blocks using the LCM method and then undergoing protein profile analysis, the key protein OPN was found. Second, in vitro, after being stimulated by OPN, the migration, proliferation, and angiogenesis of HUVECs were observed to be enhanced. The activation of Orai1/STIM1 might increase the activity of eNOS and its effect on releasing NO, which could diastole the vascular smooth muscle to increase local blood flow. Therefore, OPN could improve the function of VECs to increase the local volume of blood flow and ultimately benefit the local vessels' growth and proliferation. Third, in vivo functional experimental verified that OPN activates SOCE and promotes the healing, formation of granulation tissue, local collagen deposition, and vascular formation on the skin wound surface of diabetic mice.

stromal interaction molecule (STIM) undergoes conformational changes and oligomerization and moves to the ER-cell membrane junction to activate the highly selective calcium channel, the calcium release-activated calcium modulator (Orai), mediating the influx of extracellular Ca^{2+} [28]. Muzorewa et al. found that when SOCE activation leads to an increase in intracellular Ca^{2+} concentration, it can motivate the eNOS/NO signaling pathway, thereby improving endothelial cell function [42,43].

The OPN is the first extracellular matrix protein identified in bone tissue by Franzén A et al. [44] and plays a vital role in various cells, including osteoblasts, osteoclasts, smooth muscle cells, skeletal muscle cells, and endothelial cells. Further research has discovered that OPN not only plays a vital part in fracture healing but also promotes the proliferation and migration of endothelial cells [19,20,45] as well as local angiogenesis through the release of VEGF [8,46,47]. To investigate the mechanism of OPN and corroborate these, we overexpressed, knocked down, or re-supplemented OPN in human umbilical vein endothelial cells (HUVEC), and probed the changes in the expression of closely related molecules. Functionality tests affirmed that OPN indeed promotes endothelial cell migration and proliferation, and facilitates angiogenesis. Furthermore, by observing changes to intra- and extracellular Ca^{2+} in HUVEC upon OPN overexpression or knockdown, in addition to the participation of SOCE, we speculated that OPN contributes to activating SOCE. Similarly, Hitscherich PG et al. [48] demonstrated that SOCE activity can be inhibited by reduced expression of OPN. These findings unveil the critical pathological and physiological changes associated with OPN in the TTT process. Additionally, we directly applied OPN to facilitate wound healing in diabetic mice, marking the first observation of pathological changes caused by the activation of SOCE by OPN. This aligns with the findings of Tanaka S et al. [26] that OPN actively accelerates oral mucosal wound healing. Considering the research mentioned above, we speculated that the OPN plays a beneficial role in the wound healing process driven by TTT. As to the problem of how OPN is transported from the bone transport area to the wound area can be explained as follows: (1) From the distribution map of the local blood flow in the lower limb recorded by the laser speckle blood flow video monitoring system, an apparent increase in branches of blood flow in the area surrounding the TTT area, suggesting that angiogenesis might occur. The OPN could be transported to the wound site through the newly formed blood vessels to promote its

healing; (2) Relevant studies have shown that OPN may be transported to the target by exosomes through peripheral blood circulation [49].

However, there still exist limitations in the current research. These findings could explain the reason for the proliferation of endothelial cells during the TTT process, and supply support for the positive role of TTT in the healing of acute wounds in diabetes, but with a deficiency in revealing the connection between the TTT process and the inflammatory factors. Additionally, the wounds in this research are caused by acute injury, which may involve different pathophysiological processes from the forming and healing process triggered by chronic wounds under the hyperglycemic environment caused by diabetes. Moreover, in this study, the TTT model was carried out on healthy rats, while in further research, a diabetic rat model with the phenotype of diabetic foot would be applied for TTT modeling and experiments on chronic wound healing be conducted. Our study endeavors to elucidate the pivotal molecular biology machinations implicated in the process of transverse bone transport, particularly through the lens of endothelial cell functionality. In addition, this study aims to discover novel therapeutic targets of medicinal interventions tailored for wound repair treatment in diabetic wounds and to yield benefits for the patient to the end.

Author contributions

Lingchao Kong: Design and implement animal experiments, Methodology, Formal analysis, Investigation, Writing – original draft, Funding acquisition; Yangyang Li &; Zhongfang Deng: Methodology, Formal analysis, Investigation; Yin Xia &; Xiaoyu Chen: Design anesthesia protocols, Validation, Formal analysis; Bing Shen: Validation, Investigation; Lesha Zhang &; Rende Ning: Conceptualization, Writing – review & editing, Supervision, Project administration, Funding acquisition; Zongsheng Yin: Conceptualization, Methodology, Resources, Data curation, Writing – review & editing, Supervision, Project administration, Funding acquisition. All authors have read and agreed to the published version of the manuscript.

Ethical statement

All experimental protocols involving animals were approved by the Animal Ethics Committee at Anhui Medical University (License No. LLSC20221240) and are in accordance with the ARRIVE guidelines.

Declaration of competing interest

The authors have no conflicts of interest to declare.

Acknowledgements

We thank the Center for Scientific Research of Anhui Medical University for valuable help in our experiment.

This study was supported by grants from the Postgraduate Innovation Research and Practice Program of Anhui Medical University (grant No. YJS20230020 to L. K), the National Natural Science Foundation of China (grant No. 82372411 and No. 81871785 to Z. Y), the Natural Science Research Project of Anhui Educational Committee (grant No. 2023AH050639 to L. Z).

References

[1] Zheng Y, Ley SH, Hu FB. Global aetiology and epidemiology of type 2 diabetes mellitus and its complications. Nat Rev Endocrinol 2018;14(2):88–98.
[2] Schaper NC, van Netten JJ, Apelqvist J, Bus SA, Hinchliffe RJ, Lipsky BA, IWGDF Editorial Board. Practical Guidelines on the prevention and management of diabetic foot disease (IWGDF 2019 update). Diabetes Metab Res Rev 2020;36 (Suppl 1):e3266.
[3] Carro GV, Saurral R, Witman EL, Braver JD, David R, Alterini PA, et al. Diabetic foot attack. Pathophysiological description, clinical presentation, treatment and outcomes. Medicina (B Aires) 2020;80(5):523–30.
[4] Mariadoss AVA, Sivakumar AS, Lee CH, Kim SJ. Diabetes mellitus and diabetic foot ulcer: etiology, biochemical and molecular based treatment strategies via gene and nanotherapy. Biomed Pharmacother 2022;151:113134.
[5] Zhu YL, Guo BF, Zang JC, Pan Q, Zhang DW, Peng Y, et al. Ilizarov technology in China: a historic review of thirty-one years. Int Orthop 2022;46(3):661–8.
[6] Shevtsov VI, Shurova EN, Shurov VA. Functional outcomes of legs obliterative endarteritis treatment by Ilizarov's method. Khirurgiia 1997;(6):47–50.
[7] Zuo Q, Gao F, Song H, Zhou J. Application of Ilizarov transverse tibial bone transport and microcirculation reconstruction in the treatment of chronic ischemic diseases in lower limbs. Exp Ther Med 2018;16(2):1355–9.
[8] Ou S, Xu C, Yang Y, Chen Y, Li W, Lu H, et al. Transverse tibial bone transport enhances distraction osteogenesis and vascularization in the treatment of diabetic foot. Orthop Surg 2022;14(9):2170–9.
[9] Chang S, Zhang F, Chen W, Zhou J, Nie K, Deng C, et al. Outcomes of integrated surgical wound treatment mode based on tibial transverse transport for diabetic foot wound. Front Surg 2023;9:1051366.
[10] Nie X, Kuang X, Liu G, Zhong Z, Ding Y, Yu J, et al. Tibial cortex transverse transport facilitating healing in patients with recalcitrant non-diabetic leg ulcers. J Orthop Translat 2020;27:1–7.
[11] Jianda X, Maosheng B, Chenjian P, Xiaojing Y, Changhui W, Junhao L, et al. An novel and alternative treatment method for large heel ulceration in diabetic patients: proximal tibial cortex transverse distraction. Int Wound J 2023;20(3): 732–9.
[12] Chen Y, Ding X, Zhu Y, Jia Z, Qi Y, Chen M, et al. Effect of tibial cortex transverse transport in patients with recalcitrant diabetic foot ulcers: a prospective multicenter cohort study. J Orthop Translat 2022;36:194–204.
[13] Yuan Y, Ding X, Jing Z, Lu H, Yang K, Wang Y, et al. Modified tibial transverse transport technique for the treatment of ischemic diabetic foot ulcer in patients with type 2 diabetes. J Orthop Translat 2021;29:100–5.
[14] Wen R, Cheng X, Cao H, Zhang L, Luo F, Shang W. Transverse tibial bone transfer in the treatment of diabetes foot ulcer: a pilot study. Diabetes Metab Syndr Obes 2023;16:2005–12.
[15] Liu Z, Xu C, Yu YK, Tu DP, Peng Y, Zhang B. Twenty years development of tibial cortex transverse transport surgery in PR China. Orthop Surg 2022;14(6):1034–48.
[16] Yang Y, Li Y, Pan Q, Bai S, Wang H, Pan XH, et al. Tibial cortex transverse transport accelerates wound healing via enhanced angiogenesis and immunomodulation. Bone Joint Res 2022;11(4):189–99.
[17] Matsuyama J, Ohnishi I, Kageyama T, Oshida H, Suwabe T, Nakamura K. Osteogenesis and angiogenesis in regenerating bone during transverse distraction: quantitative evaluation using a canine model. Clin Orthop Relat Res 2005;433: 243–50.
[18] Janíček T, Hobza R, Hudzieczek V. Laser capture microdissection: from genomes to chromosomes, from complex tissue to single-cell analysis. Methods Mol Biol 2023; 2672:163–75.
[19] Icer MA, Gezmen-Karadag M. The multiple functions and mechanisms of osteopontin. Clin Biochem 2018;59:17–24.
[20] Dai J, Peng L, Fan K, Wang H, Wei R, Ji G, et al. Osteopontin induces angiogenesis through activation of PI3K/AKT and ERK1/2 in endothelial cells. Oncogene 2009; 28(38):3412–22.
[21] Kilkenny C, Browne WJ, Cuthill IC, Emerson M, Altman DG. Improving bioscience research reporting: the ARRIVE guidelines for reporting animal research. PLoS Biol 2010;8(6):e1000412.
[22] Cagle LA, Franzi LM, Epstein SE, Kass PH, Last JA, Kenyon NJ. Injectable anesthesia for mice: combined effects of dexmedetomidine, tiletamine-zolazepam, and butorphanol. Anesthesiol Res Pract 2017;2017:9161040.
[23] Limprasutr V, Sharp P, Jampachaisri K, Pacharinsak C, Durongphongtorn S. Tiletamine/zolazepam and dexmedetomidine with tramadol provide effective general anesthesia in rats. Animal Model Exp Med 2021;4(1):40–6.
[24] Griesser E, Wyatt H, Ten Have S, Stierstorfer B, Lenter M, Lamond AI. Quantitative profiling of the human substantia nigra proteome from laser-capture microdissected FFPE tissue. Mol Cell Proteomics 2020;19(5):839–51.
[25] Heydemann A. An overview of murine high fat diet as a model for type 2 diabetes mellitus. J Diabetes Res 2016;2016:2902351.
[26] Tanaka S, Yasuda T, Hamada Y, Kawaguchi N, Fujishita Y, Mori S, et al. Synthetic peptide SVVYGLR upregulates cell motility and facilitates oral mucosal wound healing. Peptides 2020;134:170405.
[27] Ungerleider JL, Johnson TD, Hernandez MJ, Elhag DI, Braden RL, Dzieciatkowska M, et al. Extracellular matrix hydrogel promotes tissue remodeling, arteriogenesis, and perfusion in a rat hindlimb ischemia model. JACC Basic Transl Sci 2016;1(1–2):32–44.
[28] Lilliu E, Koenig S, Koenig X, Frieden M. Store-operated calcium entry in skeletal muscle: what makes it different? Cells 2021;10(9):2356.
[29] Guo YN, Guo Q, Zhang Q, Ren L, Ren XY, Nie ML, et al. Proangiogenic functions of osteopontin-derived synthetic peptide RSKSKKFRR in endothelial cells and postischemic brain. Neuroreport 2021;32(15):1248–54.
[30] Zhu M, He H, Meng Q, Zhu Y, Ye X, Xu N, et al. Osteopontin sequence modified mesoporous calcium silicate scaffolds to promote angiogenesis in bone tissue regeneration. J Mater Chem B 2020;8(27):5849–61.
[31] Rotem I, Konfino T, Caller T, Schary Y, Shaihov-Teper O, Palevski D, et al. Osteopontin promotes infarct repair. Basic Res Cardiol 2022;117(1):51.
[32] Yuan Y, Liu Q, Wu Z, Luo W. Mechanistic insight on the interaction between OPN and integrin αvβ3 in osteoarthritis. BioMed Res Int 2020;2020:2905634.
[33] Harreiter J, Roden M. Diabetes mellitus: definition, classification, diagnosis, screening and prevention (Update 2023). Wien Klin Wochenschr 2023;135(Suppl 1):7–17.

[34] Muñoz-Hernández L, Márquez-López Z, Mehta R, Aguilar-Salinas CA. Intermittent fasting as part of the management for T2DM: from animal models to human clinical studies. Curr Diabetes Rep 2020;20(4):13.
[35] Shinozaki M, Okada Y, Kitano A, Ikeda K, Saika S, Shinozaki M. Impaired cutaneous wound healing with excess granulation tissue formation in TNF alpha-null mice. Arch Dermatol Res 2009;301(7):531–7.
[36] Korntner S, Lehner C, Gehwolf R, Wagner A, Grütz M, Kunkel N, et al. Limiting angiogenesis to modulate scar formation. Adv Drug Deliv Rev 2019;146:170–89.
[37] Porto Ribeiro T, Barbeau S, Baudrimont I, Vacher P, Freund-Michel V, Cardouat G, et al. Piezo1 channel activation reverses pulmonary artery vasoconstriction in an early rat model of pulmonary hypertension: the role of Ca2+ influx and akt-eNOS pathway. Cells 2022;11(15):2349.
[38] Stencel MG, VerMeer M, Giles J, Tran QK. Endothelial regulation of calmodulin expression and eNOS-calmodulin interaction in vascular smooth muscle. Mol Cell Biochem 2022;477(5):1489–98.
[39] Smith TL, Oubaha M, Cagnone G, Boscher C, Kim JS, El Bakkouri Y, et al. eNOS controls angiogenic sprouting and retinal neovascularization through the regulation of endothelial cell polarity. Cell Mol Life Sci 2021;79(1):37.
[40] Shamsaldeen YA, Lione LA, Benham CD. Dysregulation of TRPV4, eNOS and caveolin-1 contribute to endothelial dysfunction in the streptozotocin rat model of diabetes. Eur J Pharmacol 2020;888:173441.
[41] Liu TT, Xu HH, Liu ZJ, Zhang HP, Zhou HT, Zhu ZX, et al. Downregulated calmodulin expression contributes to endothelial cell impairment in diabetes. Acta Pharmacol Sin 2023;0:1–12. Epub ahead of print.
[42] Muzorewa TT, Buerk DG, Jaron D, Barbee KA. TRPC channel-derived calcium fluxes differentially regulate ATP and flow-induced activation of eNOS. Nitric Oxide 2021;111-112:1–13.
[43] Nishimoto M, Mizuno R, Fujita T, Isshiki M. Stromal interaction molecule 1 modulates blood pressure via NO production in vascular endothelial cells. Hypertens Res 2018;41(7):506–14.
[44] Franzén A, Heinegård D. Isolation and characterization of two sialoproteins present only in bone calcified matrix. Biochem J 1985;232(3):715–24.
[45] Wing TT, Erikson DW, Burghardt RC, Bazer FW, Bayless KJ, Johnson GA. OPN binds alpha V integrin to promote endothelial progenitor cell incorporation into vasculature. Reproduction 2020;159(4):465–78.
[46] Fujita N, Fujita S, Ogata N, Matsuoka M, Okada Y, Kon S, et al. Endogenous osteopontin involvement in laser-induced choroidal neovascularization in mice. Invest Ophthalmol Vis Sci 2011;52(13):9310–5.
[47] Takano S, Tsuboi K, Tomono Y, Mitsui Y, Nose T. Tissue factor, osteopontin, alphavbeta3 integrin expression in microvasculature of gliomas associated with vascular endothelial growth factor expression. Br J Cancer 2000;82(12):1967–73.
[48] Hitscherich PG, Xie LH, Del Re D, Lee EJ. The effects of macrophages on cardiomyocyte calcium-handling function using in vitro culture models. Phys Rep 2019;7(13):e14137.
[49] Bai G, Matsuba T, Niki T, Hattori T. Stimulation of THP-1 macrophages with LPS increased the production of osteopontin-encapsulating exosome. Int J Mol Sci 2020;21(22):8490.